analytical chemistry

pubs.acs.org/ac Article

Plasmonic SERS Biosensor Based on Multibranched Gold Nanoparticles Embedded in Polydimethylsiloxane for Quantification of Hematin in Human Erythrocytes

Zhewei Cai,[⊥] Yaojuan Hu,[⊥] Yujie Sun, Qingyu Gu, Ping Wu,* Chenxin Cai,* and Zijie Yan*

Cite This: https://dx.doi.org/10.1021/acs.analchem.0c03921 Read Online

ACCESS | Metrics & More | Article Recommendations | Supporting Information

ABSTRACT: This work reports a plasmonic surface-enhanced Raman scattering (SERS) biosensor that allows for quantitative analysis of hematin in erythrocytes without the need of separating it from hemoglobin (Hb). The biosensor exploits the tunable localized surface plasmon resonance (LSPR) characteristics of multibranched gold nanoparticles (M-AuNPs) and the strong plasmon coupling between an Au thin film and a flexible substrate consisting of M-AuNPs embedded in polydimethylsiloxane (PDMS) (i.e., M-AuNP-embedded PDMS substrate). In the assay, the hematin (or hematin-containing erythrocyte hemolysate) was deposited on Au film surface and covered with M-AuNP-embedded PDMS. Strong SERS signals were generated under excitation at 785 nm; the signals were sensitive to hematin concentration but not to several common coexisting biological substances. The intensities of the SERS signal (at 1623 cm^{-1}) displayed a wide linear range using hematin concentrations in a range of at least ~1.5 nM−1.1 μM; the limit of detection (LOD) was ~0.03 ± 0.01 nM at a signal/noise (S/N) of 3. This assay is simple and sensitive without tedious separation procedures, thereby saving time and enhancing efficiency. This biosensor can be used to determine hematin concentration in human erythrocyte cytosols giving concentrations of ~18.5 ± 4.5 (by averaging eight samples) and 51.5 ± 6.2 μM (by averaging three samples) for healthy and sickle erythrocytes, respectively, making it a potential application in clinical detection.

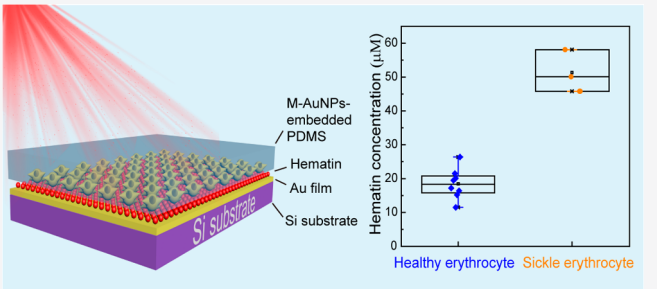

Hematin, an oxidized form of heme, is generated in erythrocytes when hemoglobin (Hb) is oxidized to met-hemoglobin (met-Hb), i.e., the iron is oxidized from Fe(II) to hydroxyl group-bound Fe(III). Once generated, it is released into the erythrocyte cytosol and has multiple harmful effects on the erythrocytes.[1,2] These effects include disrupting the integrity of the erythrocyte membrane, destroying its skeletal structure, and causing strong adhesion of sickle cells to leucocytes and endothelium. These deleterious effects call for an effective approach to measure hematin in human erythrocytes. Moreover, the accurate determination of hematin is also helpful in the design of drugs for malaria treatments.[3] However, there are a limited number of reports on the use of hematin assays to measure hematin in erythrocytes.

One of the biggest obstacles in detecting hematin in erythrocytes is the interference of Hb, since the Hb concentration (~4.4−5.6 mM) in erythrocytes is much higher than that of hematin. Most studies on heme quantification have concentrated on the total heme content, i.e., the quantities of hematin and heme.[4,5] The efforts devoted to directly quantifying hematin have been hindered owing to the lack of an effective method to separate hematin from Hb. Liu and co-workers have reported a method based on the absorption characteristics of hematin to assay hematin in healthy and sickle erythrocytes after separating hematin from Hb by ion-exchange liquid chromatography.[6] Aich and co-workers reported an enzymatic catalysis-based chemiluminescence method to quantify hematin in healthy human erythrocytes after isolation from Hb in lysed erythrocytes by dialysis.[7,8] Although the two methods are effective, they are time-consuming, since several tedious steps are required to separate hematin from Hb before the assay.

To address the separation issues, we reported a method based on the hematin-induced fluorescence quenching of boron-doped graphene quantum dots (BGQDs) to quantify hematin in human erythrocytes without the need for separation.[9] After our work, several groups used a similar method, i.e., hematin-induced fluorescence quenching of quantum dots, to quantify the hematin in erythrocytes.[10−13] However, these measurements were based on a decrease in the fluorescence signal (signal-off), thus reducing the detection

Received: September 15, 2020
Accepted: November 25, 2020

https://dx.doi.org/10.1021/acs.analchem.0c03921
Anal. Chem. XXXX, XXX, XXX−XXX

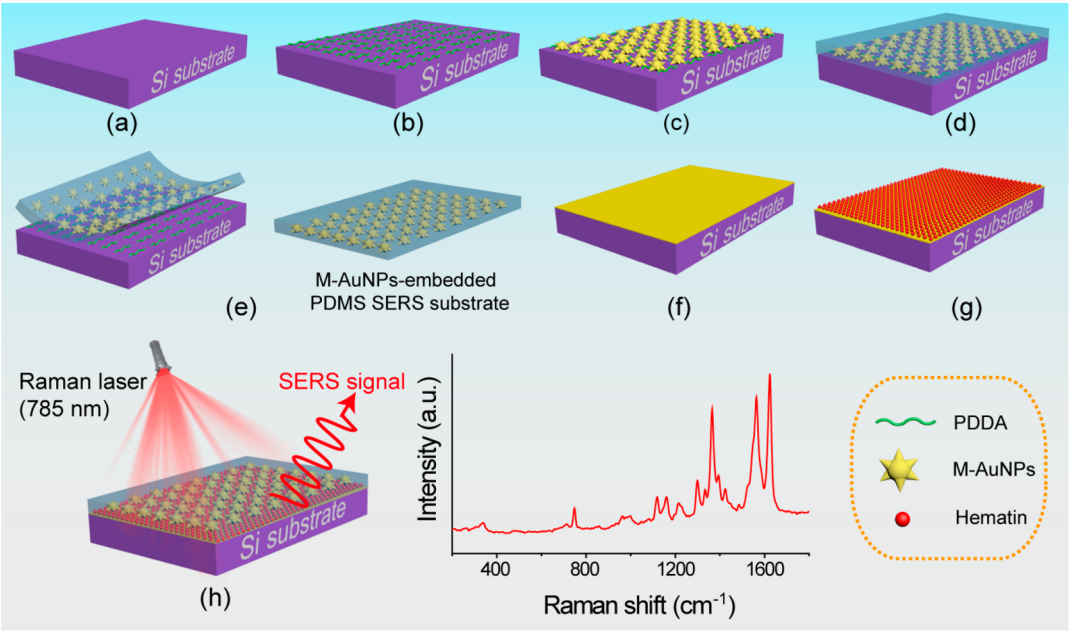

Figure 1. Biosensor fabrication. (a) Si substrate, (b) PDDA-coated Si, (c) M-AuNPs assembled on the PDDA-coated Si, (d) PDMS layer formed on the M-AuNP-assembled Si, (e) M-AuNP-embedded PDMS film, (f) Au film-coated Si, (g) hematin deposited on the Au film surface, and (h) hematin-deposited Au film covered with M-AuNP-embedded PDMS SERS active substrate.

sensitivity.[14] Therefore, to date, the sensitive and quantitative detection of hematin in erythrocytes has remained a great challenge.

Here, we report a plasmonic surface-enhanced Raman scattering (SERS) biosensor method to address this challenge. This method exploits the strong plasmon coupling features of multibranched gold nanoparticles (M-AuNPs) and their tunable localized surface plasmon resonance (LSPR) characteristics, where the former results in a strong electric field, *E*-field, and enables an enormous enhancement of the Raman signals,[15−20] while the latter can be tuned to the near-infrared region (NIR) to facilitate biological analysis.[21,22] The hematin (or hematin-containing hemolysates) is first deposited on an Au film surface and then simply covered with M-AuNP-embedded polydimethylsiloxane (PDMS) (see the biosensor configuration in Figure 1). Upon irradiation with a 785 nm laser, strong SERS signals are generated owing to the transparent and flexible features of the PDMS film, which provides the M-AuNPs with close contact with the target surface, and plasmon coupling between the M-AuNPs and the Au film.[23] The signals are directly related to the amount of hematin deposited on the Au film, which establishes the basis of the measurements. The results showed that Hb is practically SERS-inactive in the range of interest. Thus, this method meets the requirements to quantify hematin on the basis of signal increase (signal-on), without separation from Hb. All of these characteristics imply that the biosensor provides a new tool for clinical detection and disease diagnosis.

EXPERIMENTAL SECTION

M-AuNPs Synthesis and Characterization. M-AuNPs were synthesized by a seed-assisted growth method using poly(vinylpyrrolidone) (PVP) and *N*,*N*-dimethylformamide (DMF) as reducing agents.[21,23] Au seeds, with a diameter of ∼15 nm, were synthesized by reducing $AuCl_4^-$ with sodium citrate, according to a slightly modified published procedure.[24] Typically, in a condenser-equipped round-bottom flask (250 mL), 100 mL of $HAuCl_4$ (0.01 wt %) was first heated to boiling under vigorous stirring, followed by the rapid introduction of sodium citrate (3 mL, 1 wt %), causing a color change from pale yellow to burgundy. The heating mantle was removed after 10 min, and stirring was continued for 15 min. The solution was cooled to ambient temperature and filtered through a nylon membrane filter.

PVP-coated Au seeds were prepared by mixing 17.35 mL of the synthesized Au seeds with a PVP solution (25.6 mg of PVP in 1 mL of water) under stirring. After stirring for 24 h, the mixture was centrifuged, and the precipitate was dissolved in 1 mL of ethanol for the M-AuNP synthesis.

For the synthesis of M-AuNPs, $HAuCl_4$ solution (48 mM, 85 μL) was added to a PVP solution (15 mL, 8 mM, in DMF), followed by the rapid addition of the PVP-coated Au seeds (∼4 μM, 45 μL) under stirring. After stirring for 1.5 h, the produced M-AuNPs were centrifuged, washed with ethanol and water several times, and stored for biosensor fabrication.

Transmission electron microscope (TEM) images were recorded on a JEOL JEM-2100F transmission electron microscope operating at an accelerating voltage of 200 kV. Scanning electron microscopic (SEM) images were recorded using a JSM-7600F field-emitting scanning electron microscope. The extinction spectra of the synthesized M-AuNPs were recorded using a Cary 5000 UV−vis-NIR spectrophotometer (Varian).

Biosensor Fabrication. The fabrication of the biosensor is schematically illustrated in Figure 1. A Si wafer (*n*-type), with a size of 1 cm × 1 cm (Figure 1a), was cleaned, as previously reported,[25] followed by spin-coating with a thin film (∼1 nm) of positively charged poly(diallyl-dimethylammonium) (PDDA), forming a PDDA-coated Si substrate (Figure 1b). Then, a high density of the M-AuNPs ($\zeta \approx -19.6$ mV) layer was assembled by electrostatic interactions; the PDDA-coated Si was dipped in the M-AuNP solution for 24 h, producing an M-AuNP-assembled Si substrate (Figure 1c). After gently washing with deionized water and drying with N_2 blowing, the

https://dx.doi.org/10.1021/acs.analchem.0c03921
Anal. Chem. XXXX, XXX, XXX−XXX

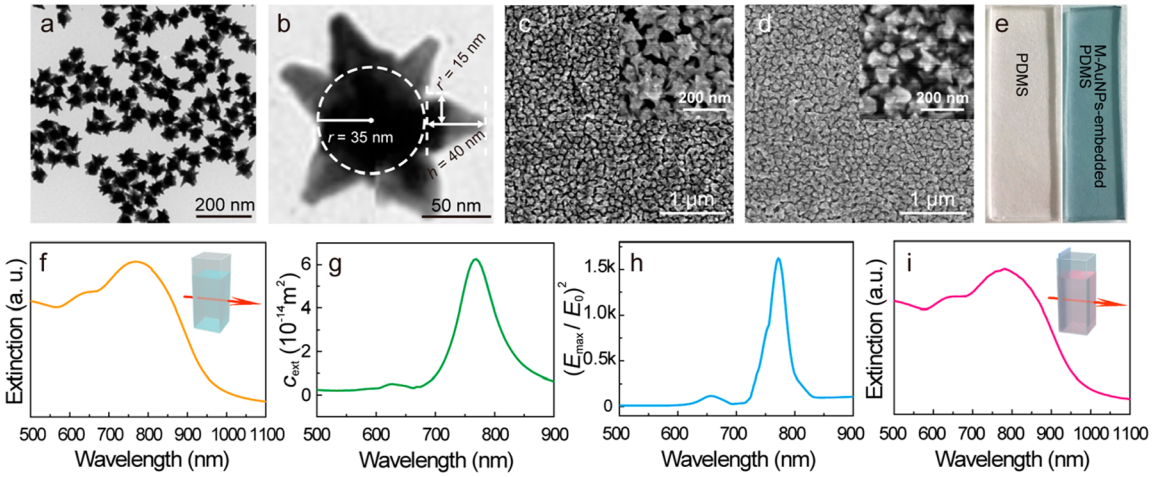

Figure 2. Morphologies and LSPR characteristics of the M-AuNPs. (a and b) TEM images of M-AuNPs, (c and d) SEM images of M-AuNPs dispersed on the Si surface (c) and embedded in PDMS (d). The insets are the images in high magnification. (e) Photographs of PDMS and M-AuNP-embedded PDMS, (f and g) experimental (f) and simulated (g) extinction spectra of M-AuNPs, (h) simulated *E*-field of M-AuNPs, and (i) experimental extinction spectra of M-AuNPs embedded in PDMS. The insets in the (f) and (i) show the configurations used to record the extinction spectra of the M-AuNPs dispersed in solution (f) and embedded in PDMS (i), respectively.

PDMS precursor, a mixture of Sylgard 184 silicon elastomer and a curing agent (at a weight ratio of 1:10),[26−28] was spin-coated and cured at ambient temperature for 24 h (Figure 1d). Finally, the PDMS film was carefully detached from the Si surface, producing the M-AuNP-embedded PDMS film (~200 μm in thickness, Figure 1e), which was used as a SERS active substrate.

For the SERS assay, Au film (~50 nm in thickness) was thermally sputtered on the cleaned Si substrate (Figure 1f) and a drop of hematin solution, of varying concentrations, was deposited on its surface, forming a layer of hematin-coated substrate (Figure 1g). After covering with the M-AuNP-embedded PDMS and irradiating with a 785 nm laser, a hematin-enhanced SERS signal was detected (Figure 1h).

SERS Measurements. The SERS spectra of the hematin or erythrocyte hemolysates were recorded using the biosensor configuration described above. The hematin solution was prepared, diluted, and spectrophotometrically determined according to our previously reported procedures.[9] Erythrocyte hemolysates (including eight samples of healthy erythrocytes and three samples of sickle cells) were prepared following the procedures reported by Aich.[7] The cells were provided by Xianlin Hospital (Nanjing, China) following a protocol approved by the Xianlin Hospital Committee for the Protection of Human Subjects. The detailed procedures for hemolysate preparation and the evaluation of the dilution compared to the cytosol are described in the Supporting Information.

In a typical SERS measurement, 20 μL of varying concentrations of hematin (0.1 nM−2.0 μM) or hemolysates was deposited on the Au film (coated on the Si substrate), which was dried and covered with the M-AuNP-embedded PDMS, and the SERS signals were collected on a Labram HR 800 microspectrometer (Jobin Yvon) under excitation at 785 nm. The spectra were typically collected within a 1 μm × 1 μm area. The Raman microscope system has a motorized stage with a precision XYZ stage controller. A 50× dark field objective with numerical aperture (NA) of 0.5 was used for signal collection. The laser power was ~10 mW, the spectrum acquisition time was 5 s, and five cycles were used. The SERS spectra were collected at 10 randomly selected points at each substrate to ensure the reproducibility of the substrate; the SERS spectra of 1 μM hematin were recorded at 10 newly prepared substrates to verify the repeatability of the substrate preparation and the assay precision.

To evaluate the selectivity of the biosensor, the SERS signals of Hb, myoglobin (Mb, also a heme-containing protein), and serum (provided by Xianlin Hospital, Nanjing, China) were also individually measured using the same procedures as those used for hematin. Considering the dilution ratios (183 in this work, see the Supporting Information) of the erythrocyte cytosols to the prepared hemolysates and the concentration of Hb in cytosols (~4.4−5.6 mM), 30 μM Hb and Mb were used in the selectivity evaluation.

RESULTS AND DISCUSSION

The aim of this work was to construct an SERS biosensor to quantify hematin in erythrocytes on the basis of the strong plasmon coupling features of M-AuNPs. For this aim, the M-AuNPs were first synthesized by employing a seed-assisted growth method, and their LSPR characteristics were characterized. In the synthesis, DMF is a weak reducing agent for the reduction of Au^{3+} to Au^{+} ions, and thus, PVP behaved as both the reducing agent, to further reduce the generated Au^{+} to Au^{0}, and the stabilizing agent for the produced Au^{0}. Moreover, PVP can guide the anisotropic growth of Au^{0} on the surface of the Au seeds to produce M-AuNPs by preferentially adsorbing on the (111) faces of the Au seeds and inhibiting further deposition of Au^{0} atoms on these faces.[21] Therefore, the morphology of the M-AuNPs can be tailored by PVP and the concentrations of the Au seeds. In order to maximize the SERS signals of the hematin assay, the goal of the synthesis was to tune the dominant LSPR peak of M-AuNPs close to 785 nm (i.e., the excitation source in the SERS measurements) to meet the requirements of the hematin assay. This was done by regulating the morphology of the M-AuNPs since their LSPR and *E*-field distribution are highly sensitive to their morphologies. The details of the morphology regulation and the corresponding extinction spectra and *E*-field

https://dx.doi.org/10.1021/acs.analchem.0c03921
Anal. Chem. XXXX, XXX, XXX−XXX

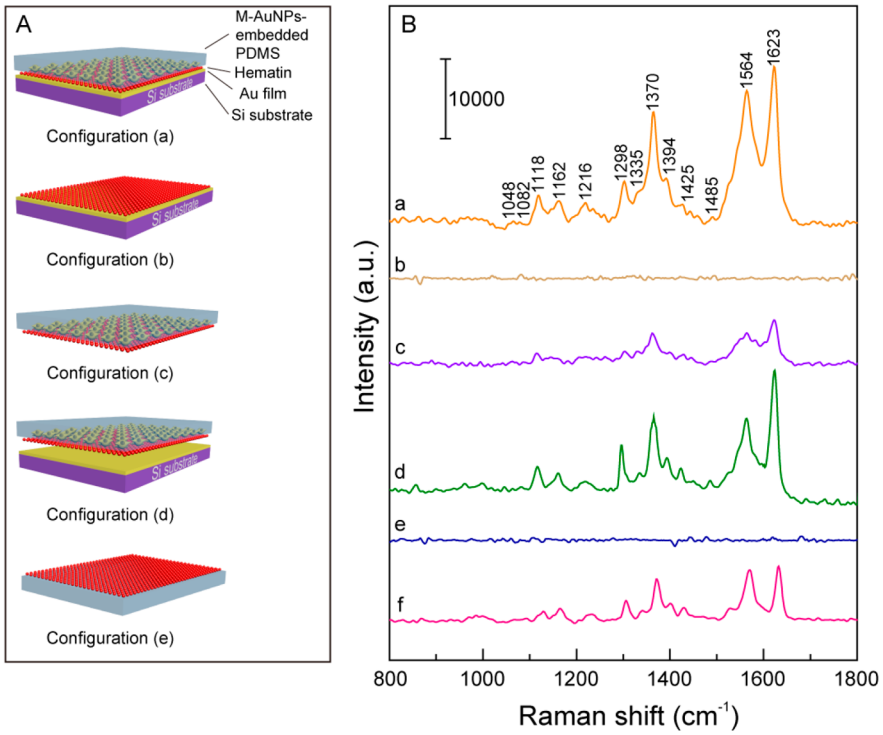

Figure 3. Biosensor configurations and the SERS spectra. (A) Different configurations of the biosensor: (a) M-AuNP-embedded PDMS covering the hematin-deposited Au film, (b) hematin deposited on the Au film, (c) hematin deposited on the M-AuNP-embedded PDMS, (d) hematin deposited on the M-AuNP-embedded PDMS covering the Au film, and (e) hematin deposited on PDMS. (B) SERS spectra of hematin recorded with the different biosensors. (a–e) SERS spectra recorded using the configurations of (a–e) in panel A, respectively, and (f) the spectrum of hematin powder. The hematin concentration is 1.0 μM. The excitation source is 785 nm.

distributions are presented in the Supporting Information and Figures S1 and S2.

The M-AuNPs that meet these requirements are monodispersed and exhibit evenly distributed features with virtually uniform morphologies (TEM, Figure 2a), consisting of an Au core (with a radius r of ~35 ± 3 nm) and six tips (with a base radius r of ~15 ± 2 nm and height h of ~40 ± 3 nm) growing around the core (Figure 2b; the histograms of the statistical analysis for the core sizes and the tip heights of the M-AuNPs are shown in Figure S3a,b, respectively). The extinction spectrum of the M-AuNPs in water displays two LSPR peaks with a strong peak at ~770 nm and a weak peak at ~635 nm (Figure 2f; the configuration for the measurement is illustrated in the inset), which correspond to the hybridization of the core and the tip longitudinal and transverse plasmon resonance modes,[21] respectively. These characteristics are in good agreement with the FDTD (finite-difference time-domain) simulated results (Figure 2g). The details of the simulation are described in the Supporting Information. The experimental spectrum exhibits a wider peak than the theoretical one; this is because the simulation usually employs monodisperse particles that do not interact with each other, while these ideal conditions cannot be met in experimentally recorded spectra. This conclusion, i.e., interactions of the particles causing a broadening of the peak of the recorded spectrum, is supported by the fact that the full width at half-maximum intensity (fwhm) of the experimental extinction spectrum of the M-AuNPs decreases at low concentrations (Figure S4).

The Raman enhancement characteristics of the nanomaterials mainly depend on the strength of the E-field. The simulated E-field is depicted in Figure 2h, where the strongest field appears at ~773 nm. This position is similar to that of the dominant peak in the extinction spectrum, as shown in Figure 2f,g. The most remarkable feature of the E-field distribution is that the wavelength of the strongest E-field is close to that of the excitation source (785 nm) that would be used in the SERS measurements. Thus, wavelength matching between the strongest E-field and the excitation was achieved, which ensures that more enhanced SERS signals would be obtained, thereby improving the assay sensitivity. Moreover, this wavelength is located in the near-infrared (NIR) region, which avoids background autofluorescence and a reduction in transmission loss of the SERS signal, and is better for the biomedical application of SERS due to the transparency of blood and tissue in this region.[29−31]

To prepare the M-AuNP-embedded PDMS, the M-AuNPs were assembled on a PDDA-coated Si surface and further embedded in PDMS. The SEM images show that the M-AuNPs were uniformly distributed on the Si surface (Figure 2c; the high-magnification SEM image is shown in the inset and Figure S5a) and were well-embedded in the PDMS film with sharp tips pointing outward (Figure 2d and its inset; the high-magnification SEM image is also shown in Figure S5b). The resulting M-AuNP-embedded PDMS displayed a uniform bluish color (Figure 2e), resembling that of the M-AuNPs in suspension. The color can clearly be distinguished from PDMS without embedded M-AuNPs (Figure 2e). These results clearly demonstrate the fabrication of the M-AuNP-embedded PDMS substrate.

To determine whether the LSPR characteristics of the M-AuNPs remained invariant after they were integrated into PDMS, the extinction spectrum of the M-AuNPs in PDMS was

https://dx.doi.org/10.1021/acs.analchem.0c03921
Anal. Chem. XXXX, XXX, XXX−XXX

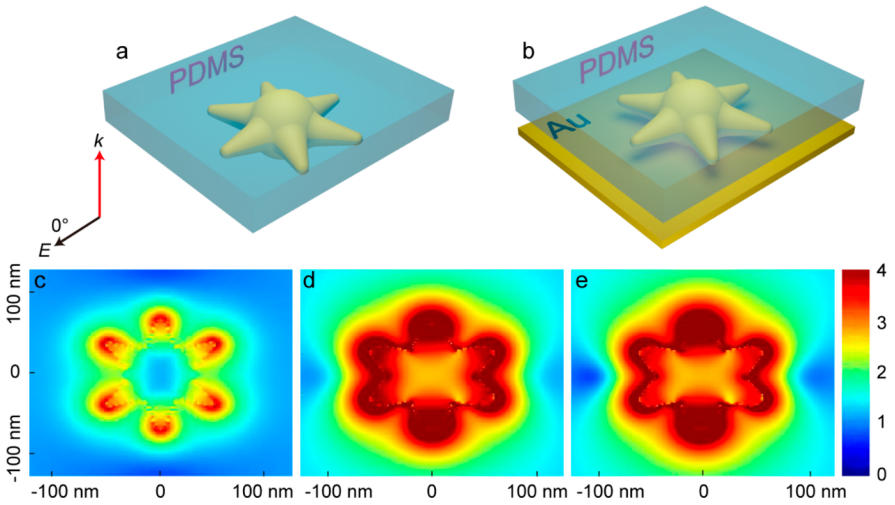

Figure 4. Distributions of the *E*-field at 785 nm in different biosensor configurations. (a) M-AuNPs embedded in PDMS. (b) M-AuNP-embedded PDMS on the Au film. The distance between the PDMS and Au film is set to be 1 nm in simulation. (c) *E*-field distribution in a vertical view for mode (a). (d and e) *E*-field distributions on PDMS (d) and Au film (e), respectively, for mode (b). The inset shows the light incident (k) and polarization directions (E). The color bar indicates the values of $\log(|E_{max}|^2/|E_0|^2)$.

recorded by immersing the M-AuNP-embedded PDMS in water in a cuvette (see the configuration in the inset, Figure 2i).[32] The spectrum (Figure 2i) reveals features similar to the spectrum of the M-AuNPs in solution (Figure 2f). The strongest extinction peak for the M-AuNPs, at ∼775 nm, is slightly red-shifted (∼5 nm) upon embedding in PDMS, due to an increase in the refractive index of the surrounding environment (from water to PDMS). These features are very important for a SERS substrate since their LSPR characteristics can be regulated in solution to meet the requirements of different excitation sources.

After synthesizing the M-AuNPs and characterizing their LSPR characteristics, the use of the M-AuNP-embedded PDMS as an SERS-active substrate for the hematin assay was evaluated by covering the hematin-deposited Au film with the M-AuNP-embedded PDMS (see biosensor fabrication in Figure 1, and configuration a in Figure 3A). Upon excitation with a 785 nm laser, strong Raman signals were observed, as shown in Figure 3B (curve a). PDMS can tightly adhere to the Au film, owing to its flexibility, and thus ensure that the embedded M-AuNPs are close enough to the hematin and Au film, which generates a strong *E*-field and results in strong SERS signals. Moreover, the PDMS is transparent and thin and has a negligible effect on the laser transmission.[33] Several characteristic Raman modes were identified by comparing the spectrum (curve a, Figure 3B) with the signals of hematin powder (curve f, Figure 3B),[34,35] for example, the band corresponding to the porphyrin skeletal vibrations of heme at ∼1623 cm^{-1}, the band relating to the totally symmetric pyrrole-ring breathing vibration (ν_4) at ∼1370 cm^{-1}, and the $C^{\beta}-C^{\beta}$ stretching vibration band at ∼1564 cm^{-1}. The band at ∼1370 cm^{-1} is usually considered as a marker for the electron density or oxidation state, since it is sensitive to the oxidation state of the iron atom within heme. Its position indicates that Fe is in the ferric high spin state. Moreover, the band at ∼1623 cm^{-1} also indicates that the high spin ferric species are six-coordinated with an exchangeable weak field distal ligand. The detailed band assignments are presented in Table S1. The Raman spectrum of hematin deposited on the Au film (configuration b, Figure 3A) does not show any observable signals (curve b, Figure 3B), which implies that the sputtered Au film is SERS-inactive for hematin, most likely due to its smooth surface. These results suggest that the AuNP-embedded PDMS can be a SERS-active substrate for hematin. More importantly, PDMS does not affect the SERS assay of hematin due to its inactivity in the range of interests (the Raman spectrum of PDMS is depicted in Figure S6).

To understand the role of the M-AuNP-embedded PDMS in the enhanced signal, the hematin was directly deposited on the surface of the M-AuNP-embedded PDMS (configuration c, Figure 3A), and the SERS signals were recorded. Although the characteristic Raman bands are observed (curve c, Figure 3B), the intensities are weaker than those recorded using configuration a (curve a, Figure 3B), implying that the coupling of the Au film with the M-AuNPs plays an important role in enhancing the SERS signal. To verify this conclusion, hematin covered M-AuNP-embedded PDMS was coated on the Au film surface (configuration d, Figure 3A). The resulting signals (curve d, Figure 3B) were much stronger than those in curve c, with intensities similar to those recorded using configuration a; this further demonstrates that the interaction of the M-AuNPs with the Au film contributes significantly to the enhancement of the SERS signal. Notably, the PDMS itself is SERS-inactive for hematin since the deposition of hematin on the PDMS surface (configuration e, Figure 3A) does not generate any SERS signal (curve e, Figure 3B).

To further understand the coupling between the Au film and the M-AuNPs embedded in PDMS, the local *E*-field distributions at 785 nm were simulated for M-AuNPs embedded in PDMS (Figure 4a) and M-AuNP-embedded PDMS covering the Au film surface (Figure 4b). These structures correspond to the biosensor configurations c and a in Figure 3A, respectively. In the case of the M-AuNPs in PDMS (Figure 4a), the strong *E*-field is only observed at the sharp tips (Figure 4c), while for the M-AuNP-embedded PDMS covering the Au film (Figure 4b), the *E*-field at the tips is significantly enhanced; moreover, the *E*-field in the gap between the adjacent tips is also quite strong (Figure 4d). Furthermore, the *E*-field on the Au film surface is also strong (Figure 4e). The trend of the simulated *E*-fields corresponds to

https://dx.doi.org/10.1021/acs.analchem.0c03921
Anal. Chem. XXXX, XXX, XXX−XXX

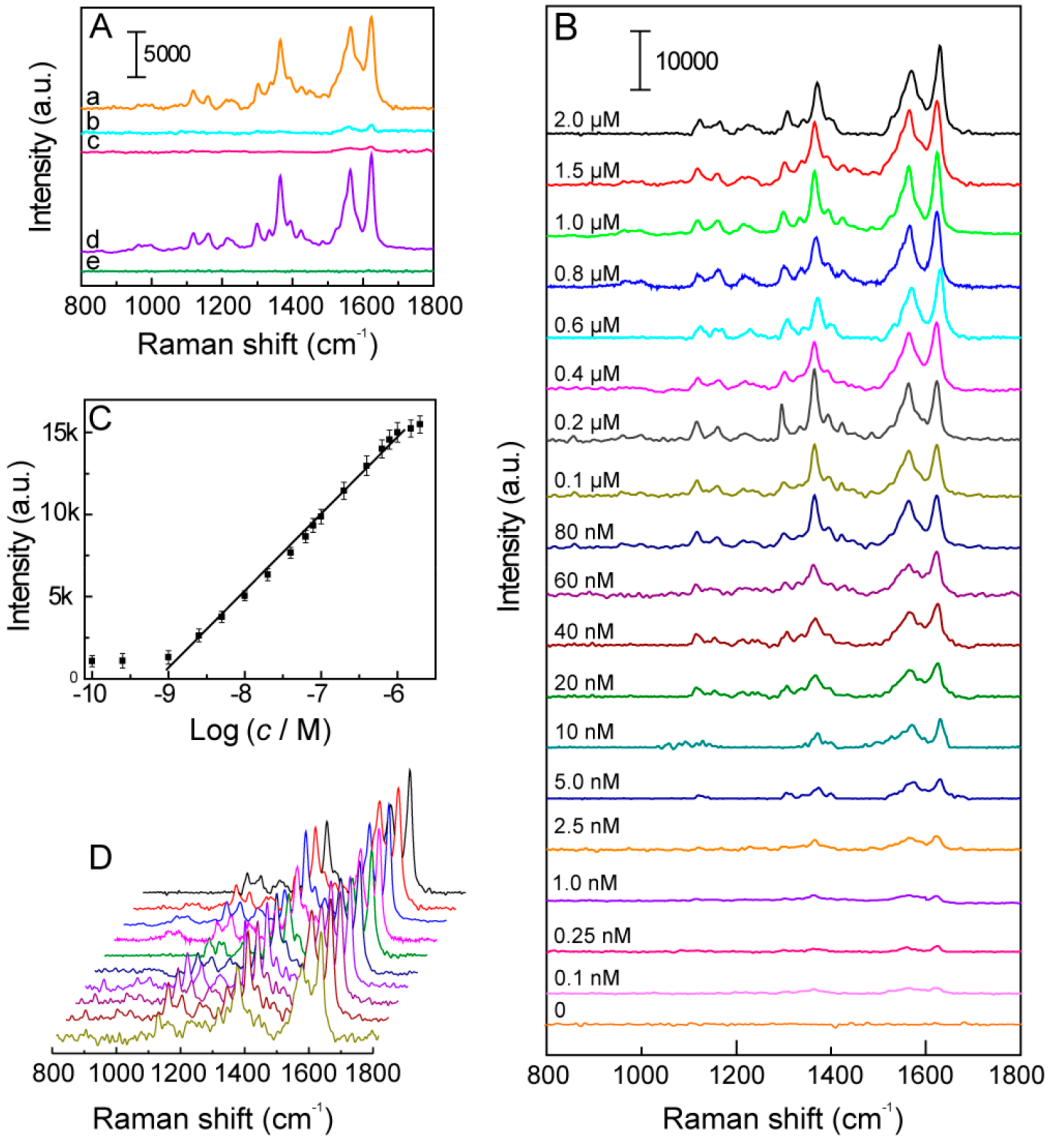

Figure 5. Performance of the biosensors. (A) SERS spectra of hematin (a, 0.3 μM), Hb (b, 30 μM), Mb (c, 30 μM), the mixture of Hb and hematin (d, 30 μM Hb + 0.3 μM hematin), and serum (e, 20 μL). (B) SERS spectra of hematin at various concentrations as indicated on each curve. (C) Dependence of the analytical signals on the hematin concentrations. The error bars are based on five measurements. (D) SERS spectra of hematin (1 μM) collected at 10 randomly selected sites. The excitation source is 785 nm.

these observed SERS signal (Figure 3B), further verifying that the strong coupling between the Au film and the M-AuNPs in PDMS plays a crucial role in the enhancement of the SERS signals.

The interference of Hb was evaluated before performing the hematin assay, due to the high concentration of Hb in erythrocyte cytosol. The results in Figure 5A (curves b, c) indicate that, although two dominant peaks are identified, the signals of both Hb and Mb (both at 30 μM) are weak and practically negligible compared to that of hematin (0.3 μM, curve a). This suggests that Hb and Mb do not interfere with the hematin assay since the amino acids of the proteins do not generate an SERS signal under the irradiation used, and the signals of heme in Hb and Mb are weak due to the amino acid shell hindering effective energy transfer.[31] This conclusion is further confirmed by the SERS spectrum of the mixture of Hb (30 μM) and hematin (0.3 μM), depicted in curve d, which indicates that the intensity of the signal of hematin in the presence of Hb has a negligible increase by considering the experimental errors (the signal of ~12600−12300, calculated from the intensity of the band at 1623 cm^{-1}) compared to that for hematin existing alone (curve a), further demonstrating that the presence of the Hb does not affect the hematin quantifying. Moreover, serum did not show clear signals (curve e, Figure 5A). These results show that the fabricated SERS biosensor has a high selectivity for hematin and could meet the assay requirements for hematin in erythrocytes.

Next, the SERS signal intensity dependence on the hematin concentration was studied, which is the basis of the hematin assay using the biosensor. The results in Figure 5B indicate that the SERS signals are sensitive to hematin concentrations. The signals increase with an increase in hematin concentration from ~0.1 nM to 2.0 μM. The dominant characteristic bands of hematin are still clearly identified at concentrations as low as 0.1 nM. The intensity of the band at 1623 cm^{-1}, corresponding to the $C_\alpha-C_m$ antisymmetric stretching, was selected as the

https://dx.doi.org/10.1021/acs.analchem.0c03921
Anal. Chem. XXXX, XXX, XXX−XXX

analytical signal. The intensities at different hematin concentrations were plotted in Figure 5C, which displays wide linear ranges with hematin concentrations between ~1.5 nM and 1.1 μM, with a low limit of detection (LOD) of ~0.03 ± 0.01 nM (at a signal/noise of 3). The linear range and LOD are better than those previously reported.[9] The reproducibility of this assay was high, as indicated by the almost invariant signals collected at 10 randomly different sites (the relative standard deviation, RSD, of ~3.8%; Figure 5D). The assay precision was also high, as demonstrated by the RSD of ~2.1% for 10 determinations of 1.0 μM hematin using newly prepared substrates.

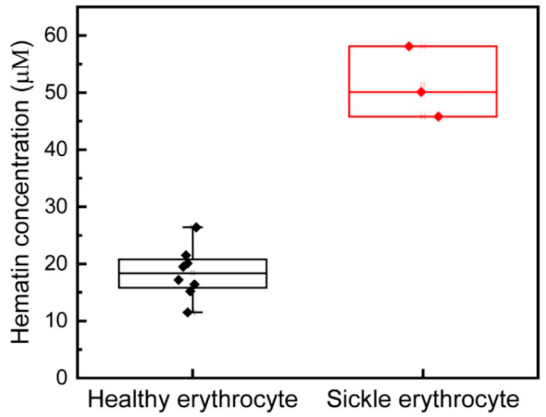

Figure 6. Practical application of the biosensor. The comparison between hematin in human healthy and sickle erythrocytes determined by the biosensor.

Moreover, the SERS biosensor can be used to assay hematin in human erythrocytes, including healthy (eight samples) and sickle cells (three samples). The SERS spectra of these cell hemolysates are shown in Figures S7 and S8. The hematin concentration in sickle cells, averaging three samples, is ~51.3 ± 6.2 μM, which is ~2.8 times that in healthy erythrocytes (~18.5 ± 4.5 μM, averaging eight samples). Note that these values of the hematin concentration in the cells are not directly read from the calibration curve in Figure 5C because the cell hemolysates were diluted by 183 times due to the high concentration of hematin in erythrocytes (the evaluation of dilution ratio of the hemolysate is described in the Supporting Information). These results are similar to those previously reported, for example, Aich et al. reported that the concentrations of hematin in sickle cells and healthy erythrocytes are 44 ± 10 and 21 ± 2 μM,[7,8] respectively, and Liu et al. reported that the hematin concentration in sickle cells is 3−5 times the value of healthy erythrocytes.[6] These results show that the fabricated biosensor can be employed as a practical platform for hematin quantification in erythrocytes.

In comparison with previously reported methods, one of the significant advantages of this assay is that no hematin separation step is required, thus saving time and enhancing the efficiency. In addition, the assay is based on the increase of the SERS signals, which increases the assay sensitivity.

CONCLUSIONS

In summary, a plasmonic SERS biosensor was constructed to quantify hematin in human erythrocytes. The SERS signals are sensitive to hematin concentrations but not to other commonly coexisting biological substances (such as Hb), exhibiting a high selectivity for hematin and highlighting that there is no need for hematin separation from Hb. The analytical signals have a good linear relationship with hematin concentrations in the range from ~1.5 nM to ~1.1 μM, with a LOD of ~0.03 ± 0.01 nM (at S/N of 3). This biosensor can be used for hematin quantification in human erythrocyte cytosols. The average concentrations of hematin in healthy and sickle erythrocyte cytosols were determined to be ~18.5 ± 4.5 and 51.5 ± 6.2 μM, respectively. One of the outstanding advantages of this method is that it does not require the separation of hematin from Hb prior to measurements, implying that it can potentially be applied in clinical detection and disease diagnosis.

It should be noted that the biosensor can only be used for assaying the total hematin in erythrocytes; it cannot determine the localized concentrations and the distributions of hematin on the cell membrane. Understanding these distributions is also important because the hematins are unevenly adsorbed by the cell membrane and be concentrated in some specific domains,[36,37] causing localized damage to membrane. Thus, a new approach should be further developed to assay or visualize the distributions of hematin on the erythrocyte membrane.

ASSOCIATED CONTENT

Supporting Information

The Supporting Information is available free of charge at https://pubs.acs.org/doi/10.1021/acs.analchem.0c03921.

Discussions of preparation of erythrocyte hemolysates, evaluation of dilution of the hemolysate, FDTD simulations, regulation of the M-AuNPs morphologies, and morphology-dependent LSPR features of the M-AuNPs, figures of TEM and SEM images, extinction and simulated extinction spectra, simulated *E*-field, distributions of core size and tip height, Raman spectrum, and SERS spectra, and table of SERS band assignments for hematin (PDF)

AUTHOR INFORMATION

Corresponding Authors

Ping Wu − *Jiangsu Key Laboratory of New Power Batteries, Jiangsu Collaborative Innovation Center of Biomedical Functional Materials, College of Chemistry and Materials Science, Nanjing Normal University, Nanjing 210023, P. R. China*; Email: wuping@njnu.edu.cn

Chenxin Cai − *Jiangsu Key Laboratory of New Power Batteries, Jiangsu Collaborative Innovation Center of Biomedical Functional Materials, College of Chemistry and Materials Science, Nanjing Normal University, Nanjing 210023, P. R. China*; orcid.org/0000-0002-3578-2415; Email: cxcai@njnu.edu.cn

Zijie Yan − *Department of Applied Physical Sciences, University of North Carolina at Chapel Hill, Chapel Hill, North Carolina 27599, United States*; orcid.org/0000-0003-0726-7042; Email: zijieyan@unc.edu

Authors

Zhewei Cai − *Department of Chemical and Biomolecular Engineering, Clarkson University, Potsdam, New York 13699, United States; Jiangsu Key Laboratory of New Power Batteries, Jiangsu Collaborative Innovation Center of Biomedical Functional Materials, College of Chemistry and*

https://dx.doi.org/10.1021/acs.analchem.0c03921
Anal. Chem. XXXX, XXX, XXX−XXX

Materials Science, Nanjing Normal University, Nanjing 210023, P. R. China

Yaojuan Hu − *School of Environmental Science, Nanjing Xiaozhuang University, Nanjing 211171, P. R. China*

Yujie Sun − *Jiangsu Key Laboratory of New Power Batteries, Jiangsu Collaborative Innovation Center of Biomedical Functional Materials, College of Chemistry and Materials Science, Nanjing Normal University, Nanjing 210023, P. R. China*

Qingyu Gu − *Jiangsu Key Laboratory of New Power Batteries, Jiangsu Collaborative Innovation Center of Biomedical Functional Materials, College of Chemistry and Materials Science, Nanjing Normal University, Nanjing 210023, P. R. China*

Complete contact information is available at: https://pubs.acs.org/10.1021/acs.analchem.0c03921

Author Contributions

[⊥]Z.C. and Y.H. contributed equally this work.

Notes

The authors declare no competing financial interest.

■ ACKNOWLEDGMENTS

This work was supported by NSFC (21405083) and NSF of the Jiangsu Province (BK20181383). Z.C. would like to thank the China Scholarship Council (CSC) for its support (201908000025).

■ REFERENCES

(1) Hargrove, M. S.; Whitaker, T.; Olson, J. S.; Vali, R. J.; Mathews, A. J. *J. Biol. Chem.* **1997**, *272*, 17385−17389.
(2) Kuross, S. A.; Rank, B. H.; Hebbel, R. P. *Blood* **1988**, *71*, 876−882.
(3) Greenwood, B.; Mutabingwa, T. *Nature* **2002**, *415*, 670−672.
(4) Qian, Y.; Xu, X.; Wang, Q.; Wu, P.; Zhang, H.; Cai, C. *Phys. Chem. Chem. Phys.* **2013**, *15*, 16941−16948.
(5) Shao, Q.; Wu, P.; Gu, P.; Xu, X.; Zhang, H.; Cai, C. *J. Phys. Chem. B* **2011**, *115*, 8627−8637.
(6) Liu, S.-C.; Zhai, S.; Palek, J. *Blood* **1988**, *71*, 1755−1758.
(7) Aich, A.; Freundlich, M.; Vekilov, P. G. *Blood Cells, Mol., Dis.* **2015**, *55*, 402−409.
(8) Aich, A.; Pan, W.; Vekilov, P. G. *AIChE J.* **2015**, *61*, 2861−2870.
(9) Ji, L.; Chen, L.; Wu, P.; Gervasio, D. F.; Cai, C. *Anal. Chem.* **2016**, *88*, 3935−3944.
(10) Ju, Y. J.; Li, N.; Liu, S. G.; Liang, J. Y.; Gao, X.; Fan, Y. Z.; Luo, H. Q.; Li, N. B. *Anal. Bioanal. Chem.* **2019**, *411*, 1159−1167.
(11) Liang, J. Y.; Han, L.; Liu, S. G.; Ju, Y. J.; Gao, X.; Li, N. B.; Luo, H. Q. *Spectrochim. Acta, Part A* **2019**, *212*, 167−172.
(12) Wu, F.-Y.; Cheng, Y.-S.; Wang, D.-M.; Li, M.-L.; Lu, W.-S.; Xu, X.-Y.; Zhou, X.-H.; Wei, X.-W. *Mater. Sci. Eng., C* **2020**, *112*, 110898.
(13) Zhang, Q. Q.; Chen, B. B.; Zou, H. Z.; Li, Y. F.; Huang, C. Z. *Biosens. Bioelectron.* **2018**, *100*, 148−154.
(14) Chen, L.; Yang, G.; Wu, P.; Cai, C. *Biosens. Bioelectron.* **2017**, *96*, 294−299.
(15) Luo, X.; Jiang, L.; Kang, T.; Xing, Y.; Zheng, E.; Wu, P.; Cai, C.; Yu, Q. *Anal. Chem.* **2019**, *91*, 7304−7312.
(16) Luo, X.; Xing, Y.; Galvan, D. D.; Zheng, E.; Wu, P.; Cai, C.; Yu, Q. *ACS Sens.* **2019**, *4*, 1534−1542.
(17) Panikar, S. S.; Ramírez-García, G.; Sidhik, S.; Lopez-Luke, T.; Rodriguez-Gonzalez, C.; Ciapara, I. H.; Castillo, P. S.; Camacho-Villegas, T.; De la Rosa, E. *Anal. Chem.* **2019**, *91*, 2100−2111.
(18) Langer, J.; de Aberasturi, D. J.; Aizpurua, J.; Alvarez-Puebla, R. A.; Auguie, B.; Baumberg, J. J.; Bazan, G. C.; Bell, S. E. J.; Boisen, A.; Brolo, A. G.; Choo, J.; Cialla-May, D.; Deckert, V.; Fabris, L.; Faulds, K.; de Abajo, F. J. G.; Goodacre, R.; Graham, D.; Haes, A. J.; Haynes, C. L.; Huck, C.; Itoh, T.; Käll, M.; Kneipp, J.; Kotov, N. A.; Kuang, H.; Le Ru, E. C.; Lee, H. K.; Li, J.-F.; Ling, X. Y.; Maier, S. A.; Mayerhöfer, T.; Moskovits, M.; Murakoshi, K.; Nam, J.-M.; Nie, S.; Ozaki, Y.; Pastoriza-Santos, I.; Perez-Juste, J.; Popp, J.; Pucci, A.; Reich, S.; Ren, B.; Schatz, G. C.; Shegai, T.; Schlücker, S.; Tay, L.-L.; Thomas, K. G.; Tian, Z.-Q.; Van Duyne, R. P.; Vo-Dinh, T.; Wang, Y.; Willets, K. A.; Xu, C.; Xu, H.; Xu, Y.; Yamamoto, Y. S.; Zhao, B.; Liz-Marzán, L. M. *ACS Nano* **2020**, *14*, 28−117.
(19) Liu, Y.; Lyu, N.; Rajendran, V. K.; Piper, J.; Rodger, A.; Wang, Y. *Anal. Chem.* **2020**, *92*, 5708−5716.
(20) Qi, G.; Wang, D.; Li, C.; Ma, K.; Zhang, Y.; Jin, Y. *Anal. Chem.* **2020**, *92*, 11755−11762.
(21) Hu, Y.; Liu, X.; Cai, Z.; Zhang, H.; Gao, H.; He, W.; Wu, P.; Cai, C.; Zhu, J.-J.; Yan, Z. *Chem. Mater.* **2019**, *31*, 471−482.
(22) Xing, Y.; Cai, Z.; Xu, M.; Ju, W.; Luo, X.; Hu, Y.; Liu, X.; Kang, T.; Wu, P.; Cai, C.; Zhu, J.-J. *Chem. Sci.* **2019**, *10*, 10900−10910.
(23) Pu, Y.; Zhao, Y.; Zheng, P.; Li, M. *Inorg. Chem.* **2018**, *57*, 8599−8607.
(24) Graf, C.; Vossen, D. L. J.; Imhof, A.; van Blaaderen, A. *Langmuir* **2003**, *19*, 6693−6700.
(25) Liang, W.; Wu, C.; Cai, Z.; Sun, Y.; Zhang, H.; Wu, P.; Cai, C. *Chem. Commun.* **2019**, *55*, 2853−2856.
(26) Fortuni, B.; Fujita, Y.; Ricci, M.; Inose, T.; Aubert, R.; Lu, G.; Hutchison, J. A.; Hofkens, J.; Latterini, L.; Uji-I, H. *Chem. Commun.* **2017**, *53*, 5121−5124.
(27) Lu, G.; Li, H.; Zhang, H. *Small* **2012**, *8*, 1336−1340.
(28) Wen, X.; Li, G.; Zhang, J.; Zhang, Q.; Peng, B.; Wong, L. M.; Wang, S.; Xiong, Q. *Nanoscale* **2014**, *6*, 132−139.
(29) Gao, J.; Wu, C.; Deng, D.; Wu, P.; Cai, C. *Adv. Healthcare Mater.* **2016**, *5*, 2437−2449.
(30) Wen, S.; Miao, X.; Fan, G.-C.; Xu, T.; Jiang, L.-P.; Wu, P.; Cai, C.; Zhu, J.-J. *ACS Sens.* **2019**, *4*, 301−308.
(31) Wu, P.; Deng, D.; Gao, J.; Cai, C. *ACS Appl. Mater. Interfaces* **2016**, *8*, 10243−10252.
(32) Shiohara, A.; Langer, J.; Polavarapu, L.; Liz-Marzán, L. M. *Nanoscale* **2014**, *6*, 9817−9823.
(33) Park, S.; Lee, J.; Ko, H. *ACS Appl. Mater. Interfaces* **2017**, *9*, 44088−44095.
(34) Wood, B. R.; Bailo, E.; Khiavi, M. A.; Tilley, L.; Deed, S.; Deckert-Gaudig, T.; McNaughton, D.; Deckert, V. *Nano Lett.* **2011**, *11*, 1868−1873.
(35) Yeo, B.-S.; Mädler, S.; Schmid, T.; Zhang, W.; Zenobi, R. *J. Phys. Chem. C* **2008**, *112*, 4867−4873.
(36) Asakura, T.; Agarwal, P. L.; Relman, D. A.; McCray, J. A.; Chance, B.; Schwartz, E.; Friedman, S.; Lubin, B. *Nature* **1973**, *244*, 437−438.
(37) Hebbel, R. P. *Clin. Haematol.* **1985**, *14*, 129−140.